



HAL
open science

Reappraisal of Upscaling Descriptors for Transient Two-Phase Flows in Fibrous Media

Aubin Geoffre, Nicolas Moulin, Julien Bruchon, Sylvain Drapier

► **To cite this version:**

Aubin Geoffre, Nicolas Moulin, Julien Bruchon, Sylvain Drapier. Reappraisal of Upscaling Descriptors for Transient Two-Phase Flows in Fibrous Media. *Transport in Porous Media*, 2023, 147 (2), pp.345 à 374. 10.1007/s11242-023-01912-w . emse-04257598

HAL Id: emse-04257598

<https://hal-emse.ccsd.cnrs.fr/emse-04257598>

Submitted on 15 Apr 2024

HAL is a multi-disciplinary open access archive for the deposit and dissemination of scientific research documents, whether they are published or not. The documents may come from teaching and research institutions in France or abroad, or from public or private research centers.

L'archive ouverte pluridisciplinaire **HAL**, est destinée au dépôt et à la diffusion de documents scientifiques de niveau recherche, publiés ou non, émanant des établissements d'enseignement et de recherche français ou étrangers, des laboratoires publics ou privés.

Reappraisal of upscaling descriptors for transient two-phase flows in fibrous media

Aubin Geoffre^{1*}, Nicolas Moulin^{1†}, Julien Bruchon^{1†}
and Sylvain Drapier^{1†}

^{1*}Hexcel Industrial Chair - Mines Saint-Étienne, Université de
Lyon, CNRS, UMR 5307 LGF, Centre SMS, 158 Cours Fauriel,
Saint-Étienne, 42023, France.

*Corresponding author(s). E-mail(s): a.geoffre@emse.fr;
Contributing authors: nmoulin@emse.fr; bruchon@emse.fr;
drapier@emse.fr;

†These authors contributed equally to this work.

Abstract

Transient two-phase flows within fibrous media are considered at local scale. Upscaling these flows constitute a key procedure towards a tractable description in an industrial context. However, the task remains challenging as a time-dependent behaviour is observed within a geometrically complex structure with interplay of various physical phenomena (capillary effects, viscous dissipation,...). **The usual upscaling strategies, encountered in both soil sciences and composite materials communities are reviewed, compared, and finally adapted to reach a method that is relevant to describe fibrous media imbibition. Using finite element flow simulations on statistical representative volume elements, the proposed approach first considers several definitions for saturation in order to characterise the flow dynamics as well as the characteristic length associated with the transient behaviour.** Next, two methods are proposed to assess a resulting capillary pressure, demonstrating the importance to properly define the capillary pressure acting on the interface. The first one considers the mean pressure jump at the interface while the second one uses a machine-learning technique, namely Gaussian Process Regression, to retrieve the mean curvature of the interface. Those methods are found to be both consistent and in agreement with the results from the literature.

001
002
003
004
005
006
007
008
009
010
011
012
013
014
015
016
017
018
019
020
021
022
023
024
025
026
027
028
029
030
031
032
033
034
035
036
037
038
039
040
041
042
043
044
045
046

047 Finally, a novel approach that stochastically describes the position of the
 048 flow front through a presence distribution is detailed. The spread of the
 049 front can be compared to the saturation length and its value has been
 050 found to be small enough to be neglected at upper scale, justifying the
 051 use of sharp interface models for similar porous media and flow settings.

052 **Keywords:** Upscaling, Capillary pressure, Two-phase flow simulations,
 053 Gaussian Process Regression

058 Notations and abbreviations (text order)

062	RVE	Representative Volume Element
063		
064	S_L	Liquid saturation of the volume
065	S_L^{max}	Maximum liquid saturation of the volume
066		
067	t	Time variable
068		
069	Ca	Capillary number
070		
071	η_i	Viscosity of phase i
072	v_{in}	Inlet velocity
073		
074	γ_j	Surface tension coefficient of interface j
075		
076	P_{vol}^c	Resulting capillary pressure (volume definition)
077	p	Fluid pressure field
078		
079	$\langle \cdot \rangle^i$	Volume averaging operator over phase i
080		
081	Ω_i	Domain associated with phase i
082	$ \omega $	Volume/surface of domain ω
083		
084	$P_{vol,dyn}^c$	Dynamic capillary pressure (volume definition)
085		
086	τ	Relaxation coefficient associated with $P_{vol,dyn}^c$
087	$[[p]]_j$	Pressure jump at interface Γ_j
088		
089	\mathcal{C}	Mean curvature
090	$\langle \cdot \rangle^{LV}$	Surface averaging operator over the liquid-vapor interface Γ_{LV}
091		
092		

P_p^c	Resulting capillary pressure (pressure jump definition)	093
P_C^c	Resulting capillary pressure (mean curvature definition)	094
Ω	Computational domain	095
ρ_i	Density of phase i	096
\bar{r}	Average fibre radius	097
\mathbf{v}	Fluid velocity field	098
ϕ	Level-set field	099
ASGS	Algebraic SubGrid Scale	100
SUPG	Streamline Upwind Petrov-Galerkin	101
V_f	Fibre volume ratio	102
SRVE	Statistical Representative Volume Element	103
L	Characteristic length of the computational domain	104
$s_L(A)$	Liquid saturation of section A	105
$s_L^{max}(A)$	Maximum liquid saturation of section A	106
R	Ratio between $s_L(A)$ and $s_L^{max}(A)$	107
ℓ_s	Saturation length	108
GPR	Gaussian Process Regression	109
\mathcal{F}	Area containing the flow front	110
$\mathbf{x}_i^{\mathcal{F}}$	Coordinates of the vertices that shape the flow front	111
$I_{\mathbf{x}_{\mathcal{F}}}$	Random variable which realisations give $\mathbf{x}_i^{\mathcal{F}}$	112
ℓ_s^*	Saturation length averaged over time	113
P_p^{c*}	Asymptotic value of P_p^c	114
P_C^{c*}	Asymptotic value of P_C^c	115
μ	Mean value of the flow front distribution	116
σ	Standard deviation of the flow front	117
σ^*	Asymptotic value of σ	118
		119
		120
		121
		122
		123
		124
		125
		126
		127
		128
		129
		130
		131
		132
		133
		134
		135
		136
		137
		138

1 Introduction

Multiphase flows in fibrous media are commonly observed in numerous fields going from soil science [1–3] to composite manufacturing processes [4, 5] where a carbon fibre preform that initially contains rarefied air is filled with a liquid resin. A multiphase flow resin/air within a porous fibrous medium is thus observed. This medium naturally shows several scales of description, starting from the scale of the carbon fibre ($\sim \mu\text{m}$) to the scale of the industrial part ($\sim \text{m}$). As flow models must be adapted to the scale of representation, connecting those microscopic and macroscopic scales has been a major concern in the scientific community. As a first approach, a permeability tensor that represents the ability of the fibrous structure to be crossed by a fluid is generally studied. This concept has been first introduced following Darcy’s works to macroscopically describe a monophasic steady flow in a porous medium [6]. Besides, the complexity of a multiphase flow can hardly be reduced to a single tensor. Such flows are indeed considerably more challenging to describe as several phases are observed with a moving interface. The observed behaviour becomes non-linear, time-dependent and sensitive to many parameters such as fluid properties or boundary conditions. In addition to this, the vicinity between carbon fibres, around few micrometers, leads to consider capillary effects and consequently a sensitivity to surface tension coefficients [7, 8].

From early theoretical works, upscaling strategies from Representative Volume Elements (RVE) have been proposed to transpose the microscopic description of multiphase flows in porous media towards an upper scale [3, 9–11]. Those have been mainly developed by the hydrogeology community for the study of flows within soils or rocks. Later on, the composite materials community have developed its own approaches, that are particularly suited for the study of fibrous materials impregnation but that may suffer from a lack of

sound theoretical ground. The novelty of this contribution consists in operating an explicit connection between both types of approaches, so as to retrieve a rigorous, precise, and complete description that is adapted to the imbibition of fibrous media while carrying the specificities and constraints inherent to composite materials.

1.1 Saturation

The most straightforward upscaling quantity is the liquid saturation $S_L \in [0, 1]$ that describes the proportion of liquid within the poral space. As imbibition is considered here, S_L increases over time from 0 to a maximal value $S_L^{max} = S_L(t \rightarrow \infty)$ obtained when the two-phase flow reaches steadiness. The relation $S_L = S_L(t)$ characterises the global dynamics of the flow. The asymptotic saturation value S_L^{max} is lower than 1 as the flow tends to entrap air bubbles behind the front. This proportion of residual phase at final state is a concern in many fields since it can be associated with a recovery ratio in hydrology [12] or a void content in the composite materials community [13]. As bubble entrapment phenomenon results from velocity inhomogeneity over the volume, S_L^{max} value is expected to be directly dependent on the competition between viscous and capillary effects. This is expressed through the capillary number Ca that is defined here as:

$$Ca = \frac{\eta_L v_{in}}{\gamma_{LV}} \quad (1)$$

where η_L is the liquid viscosity, v_{in} the inlet velocity and γ_{LV} the surface tension coefficient from the liquid-vapor interface.

Studying the saturation finally describes a complex phenomenon through a single time-dependent scalar. It is especially convenient at upper scales where the two-phase flow can be modeled as a transport of saturation in an equivalent homogeneous medium [14]. However, in the context of an upscaling procedure,

231 a global saturation only provides a rough description of the flow without spa-
232 tial information. As a consequence, a first improvement consists in defining
233 saturation at a more local scale. This is observed in the literature related to
234 composite materials processes where local saturation curves are often consid-
235 ered [15–19], they consist in representing saturation as a function of position
236 at a given time. A transition between two saturation regimes is observed, its
237 characteristic width is referred to as *saturation length*. This approach is par-
238 ticularly suited for the type of flow and geometry under consideration, that is
239 to say the impregnation of fibrous reinforcements as encountered in aeronau-
240 tical structural applications and that locally show a statistically homogeneous
241 nature. It thus may be complex to transpose to other specific contexts, like
242 wicking in 3D structures, where further difficulties arise, such as pore delays
243 [20].

257 1.2 Capillary effects

259 Capillary effects rising from surface tension phenomena act as a complemen-
260 tary force in the filling of fibrous microstructures. However, in a more general
261 context, it depends on the fluids under consideration as well as the pore struc-
262 ture. In the context of manufacturing processes of composite materials, it is
263 generally considered as a driving force that helps the impregnation [7]. In
264 any case, this contribution has to be upscaled. This is achieved through the
265 introduction of a *resulting* capillary pressure P^c . Though the *capillary pres-*
266 *sure* term is widely encountered in literature, it may admit several definitions
267 and approaches. In literature and especially in the hydrogeology community,
268 it is generally defined at the volume scale [21]. A first definition P_{vol}^c is thus
269 obtained as the difference between volume-averaged phase pressure:

$$P_{vol}^c = \langle p_V \rangle^V - \langle p_L \rangle^L \quad (2)$$

where p_i is the pressure field associated to phase i . From now on, L will refer to the liquid phase, V to the vapor phase and S to the solid one. Such a definition (Eq.2) requires volume-averaging operator:

$$\langle \cdot \rangle^i = \frac{1}{|\Omega_i|} \int_{\Omega_i} \cdot dV \quad (3)$$

Those volume-defined capillary pressures are generally expressed as a function of the saturation S_L [22]. The determination of capillary pressure-saturation curves constitutes a huge area of research as they are considered to characterise the two-phase flow at a macroscopic level. They finally provide a simple macroscopic relation that is convenient to use in practice especially when transport of saturation is considered.

However, obtaining capillary pressure-saturation curves is challenging for several reasons. First, an hysteresis phenomenon is classically observed between the imbibition and drainage curves [23]. Besides, it has been shown that equilibrium must be reached so that Eq.2 match the capillary pressure [24, 25]. This especially makes the experimental determination of $P_{vol}^c - S_L$ curves very time-consuming since for a given saturation value, the flow may take several hours to stabilise towards a steady state [26]. In parallel, flows observed in practice generally show a transient behaviour where the static equilibrium is never met. This finally leads to consider *dynamic capillary effects* for which a considerable amount of contribution can be found [23, 27, 28]. In the context of these works, the instantaneous difference of phase pressure $P_{vol,dyn}^c$ is then measured and related to the static pressure through the (de)saturation rate

323 [21]:

$$324 \quad P_{vol,dyn}^c = P_{vol}^c - \tau \frac{\partial S_L}{\partial t} \quad (4)$$

325
326 where the dynamic coefficient τ controls the rate to reach the equilibrium.
327 The value for this coefficient can span several orders of magnitude and its
328 dependancies are complex and still on study [23, 27–30]. It should be noticed
329 that $P_{vol,dyn}^c$ is sometimes referred to as *dynamic capillary pressure* which is
330 somehow ambiguous as the quantity does not rely on any rigorous justification
331 based on capillary laws.
332
333
334
335
336
337
338

339 1.3 Interfacial capillary pressure

340
341 In spite of its apparent simplicity and the convenience of its use, a capillary
342 pressure-saturation relationship can finally be complex to determine and raise
343 numerous modelling questions. More generally, assuming that capillary effects
344 match a global difference between phase pressures is not straightforward [31].
345 Mathematically, capillary action is taken into account through the Laplace's
346 law (Eq.5) that only holds at the interface between two phases:
347
348
349
350
351

$$352 \quad \llbracket p \rrbracket_j = \gamma_j \mathcal{C} \quad \text{in} \quad \Gamma_j(t) \quad (5)$$

353
354
355 where $\llbracket p \rrbracket_j$ is the pressure field discontinuity at interface Γ_j , characterised by
356 its surface tension γ_j and by a mean curvature \mathcal{C} .

357
358 As a consequence, a rigorous upscaling procedure cannot retrieve a volume
359 definition of capillary pressure. All these arguments lead to reevaluate the com-
360 mon volume definition of capillary pressure. To be consistent with the physics
361 of the problem, as well as the upscaling procedure, a resulting capillary pres-
362 sure computed at the interface level should be considered [25, 32]. Starting
363 from Eq.5, a surface averaging over the liquid-vapor interface can be carried
364
365
366
367
368

out through an operator $\langle \cdot \rangle^{LV}$:

$$\langle \cdot \rangle^{LV} = \frac{1}{|\Gamma_{LV}|} \int_{\Gamma_{LV}} \cdot dS \quad (6)$$

This gives two other approaches for considering resulting capillary pressure.

A first one consists in averaging the pressure jump [33, 34] while the second integrates the mean curvature over the interface [11, 24, 34, 35]:

$$P_p^c = \langle \llbracket p \rrbracket_{LV} \rangle^{LV} \quad (7)$$

$$P_C^c = \gamma_{LV} \langle \mathcal{C} \rangle^{LV} \quad (8)$$

As capillary pressure becomes defined at interface level, its dependancies to time or saturation can be reappraised. Indeed, capillary pressure does not correspond anymore to a volume scale driving force that may depend on the proportion of each phase. Instead, the resulting capillary action can be expected to be only a function of the porous geometry and surface tension coefficients. This is in agreement with the composite materials literature [7, 36] in which capillary pressure is considered as an intrinsic property of the porous medium and fluids.

1.4 Description of the flow front

Finally, a novel method to characterise the flow front is proposed in this work. As the flow front is fragmented and discontinuous within the complex poral structure, modeling it in a deterministic way may be criticised [19]. Consequently, a statistical modelling is proposed where the flow front is characterised by a presence distribution. At an upper scale, this allows us to

415 assess the mean position of the flow front as well as its spread across the poral
416 structure, which is particularly relevant in the study of complex porous media.
417

418

419

420 This paper will first recall the numerical strategy for the simulation of
421 transient two-phase flow (Section 2.1). Next, the proposed upscaling procedure
422 will be detailed (Section 2.2). Then the results will be presented (Section 3)
423 and discussed (Section 4).
424

425

426

427

428

429

2 Materials and methods

430

431 The physical modelling of transient two-phase flow is now detailed. Such a
432 problem is solved within a stabilised finite element framework that has been
433 presented in previous studies and that will be briefly recalled here. Particu-
434 liar attention is paid to the generation method of fibrous geometries and to
435 boundary conditions. Then the proposed upscaling method will be explained.
436

437

438

439

440

441

442

2.1 Numerical simulation of a two-phase flow within a fibrous medium

443

444

445

446

2.1.1 Physical problem and conservation laws

447 Two-phase flows with a moving interface are here adressed by solving two
448 coupled problems. The first one corresponds to the fluid problem and consists
449 in solving mass and momentum conservation equations on the computational
450 domain Ω (Fig.1). Both liquid and vapor phases are assumed to be newtonian
451 fluids and the flow incompressible. As the invading phase under consideration
452 shows a high viscosity and low velocity, a sufficiently low Reynolds number
453 can be assumed:
454

455

456

457

458

459

460

$$Re = \frac{2\bar{r}\rho_L v_{in}}{\eta_L} \ll 1 \quad (9)$$

where ρ_L is the liquid density and \bar{r} the average fibre radius. Consequently, the convective and transient terms of Navier-Stokes' equations can be discarded. As a consequence, Stokes equations are here considered [37]. Let us consider that phase $i \in \{L, V\}$ occupies a domain $\Omega_i(t)$ at time t . The following problem is solved:

$$\left. \begin{aligned} \nabla \cdot \mathbf{v} &= 0 \\ \eta_i \Delta \mathbf{v} - \nabla p &= 0 \end{aligned} \right\} \text{ in } \Omega_i(t) \quad (10)$$

As an interface condition, no-slip is prescribed on the fibres.

Capillary effects are taken into account through Laplace's relationship already introduced in Eq.5 where $j \in \{LV, LS, SL\}$ (Fig.1). The contributions associated to the solid phase in Eq.5 vanish, as the fibres are supposed to be non-deformable. As a numerical consequence, the solid domain Ω_S is not meshed. Surface tension coefficients and viscosities are chosen to be consistent with experimental measurements [38] encountered in direct manufacturing processes of composite materials, and can be found in Table 1.

The model requires to locate the phases and the liquid-vapor interface Γ_{LV} in order to compute capillary terms or to apply the proper fluid properties. The interface is here modeled implicitly with a level-set method. The method leans on a scalar field ϕ that describes the signed distance between each point of the computational domain and the liquid-vapor interface [39]. Therefore the zero iso-value of the field corresponds to the liquid-vapor interface. **The whole field is then convected in the fluid velocity field \mathbf{v} to describe the moving interface [37]:**

$$\frac{\partial \phi}{\partial t} + \mathbf{v} \cdot \nabla \phi = 0 \quad \text{in } \Omega \quad (11)$$

with $\Omega = \Omega_L \cup \Omega_V$. **The resolution of Eq.11 requires both initial and boundary conditions. The initial level-set field corresponds to a plane liquid/vapor**

507 interface, close to the inlet boundary. A boundary condition, usually on the
508 inlet boundary, is prescribed as a non-zero constant value for which the sign
509 indicates which phase enters the volume. Finally, to ensure that the field ϕ re-
510 mains a distance function throughout the computation, a reinitialisation step
511 is performed [40, 41].
512
513

516 **2.1.2 Numerical strategy for solving the physical problem**

518 The problem described in the previous section (Eqs. 10,11) is solved with a
519 finite element approach through an in-house implementation in Z-set software¹.
520 The validity of the numerical strategy has been proved in various contributions
521 [37, 42–48]. The fluid problem is solved using linear approximations for both
522 velocity and pressure fields, associated with an ASGS strategy [49, 50]. The
523 implementation of capillary conditions at interfaces will not be detailed here
524 but further explanations can be found in [43]. Then, the level-set field is also
525 approximated by linear functions and its convection (Eq.11) is stabilised by a
526 SUPG method [51]. Both fluid and level-set problems share the same mesh and
527 are weakly coupled. An exemple of simulation within a fibrous microstructure
528 is represented in Fig.2.
529
530
531
532
533
534
535
536

537 **2.1.3 Generation of fibrous microstructures**

540 The porous medium under consideration is made of long carbon fibres. As a
541 consequence, it is common to work within the plane that is tranverse to the
542 fibre axis [46]. This leads us to consider a 2D flow around a set of disks.
543 Fibrous microstructures have thus been randomly generated, from an input
544 value of fibre volume ratio V_f , and through an algorithm detailed in a previous
545 contribution [46]. In that paper, it was shown that the generated microstruc-
546 tures are statistically representative of real fibrous structures with respect
547
548
549
550

551 ¹<http://www.zset-software.com/>
552

to both mechanical response and geometrical considerations. In that sense, the microstructures can be considered as Statistical Representative Volume Elements (SRVE) [52]. The geometries are thus able to grasp the inherent randomness of the medium. To our knowledge, studying the impregnation of fibrous media from such volumes through transient two-phase flow simulations is a novelty, as similar studies are generally based on idealised representations of fibrous structures, using unit cells for instance.

In [46], a (S)RVE size has been determined for permeability considering steady flow simulations. It has been remarked that RVE is met for a size L such that $L/\bar{r} \approx 80$. However, for significantly lower value of L/\bar{r} , the results have been found to yield permeabilities very close to the asymptotic value. As a result, the RVE size has been set at 50 as a satisfactory trade-off between the statistical representativity and the computation cost. Fibre density will be kept here at 50% to consider an intermediate value.

2.2 Upscaling methods

2.2.1 Saturation

Saturation S_L is defined here as the proportion of liquid volume $|\Omega_L|$ over the overall poral volume $|\Omega|$:

$$S_L = \frac{|\Omega_L|}{|\Omega|} \quad (12)$$

It is thus defined at the volume scale and gives a global characterisation of the flow. Its temporal evolution translates the overall dynamics of the flow. It especially depends on the flow control that is prescribed through inlet/outlet boundaries of the volume (Fig.3). The imbibition of the fibrous structure is mainly driven by the boundary conditions prescribed at the inlet/outlet boundaries. Depending on whether a pressure drop or a flow rate is prescribed, the dynamics of impregnation can be significantly different. Consequently, as

discussed in the next paragraph, the type of flow control influences directly the time evolution of S_L .

When the same constant flow rate is prescribed at the inlet/outlet boundaries, the time evolution of S_L is first linear as the incompressible fluid is forced to travel the same distance at any time (Fig.3). Then, saturation converges towards an asymptotic value S_L^{max} as the flow reaches steadiness. On the contrary, if a pressure drop between the inlet and outlet boundaries is prescribed, the time evolution of S_L is non-linear and a clear transition between flow regimes is complex to identify. As the liquid fills the pore space, the overall volume viscosity increases and the fluid displacement induced by the pressure drop becomes increasingly smaller. Consequently, the average fluid velocity may drop by several orders magnitude between the beginning and the end of the simulation. This may alter the flow behaviour over time, particularly the competition between viscous and capillary effects which is represented through the capillary number Ca [53] (Eq.1).

In infusion-based manufacturing processes for composite materials, a pressure drop is imposed at the industrial part scale. At the local scale under consideration, this would lead to prescribe different pressure values on opposite sides of the domain. However, the aim of this study is to characterise the upscaling of local flows. For this purpose, it seems necessary to have a strong control on the flow regime throughout the simulation: a flow rate control will be prescribed on the volume in the rest of the study. A wall condition (i.e. $\mathbf{v} = \mathbf{0}$) is applied on the boundaries that are parallel to the imposed flow. Note that, although the microstructure is periodic, no periodic boundary condition has been used here. Indeed, in the case of a two-phase flow a periodic boundary condition should ensure the periodicity of the velocity, but should also guarantee that the same phase is considered on the corresponding nodes of both boundaries.

644

Since the mechanical response is supposed to be independent of such boundary conditions as soon as the geometry can be regarded as a RVE, which is the case here [46], wall conditions have been considered throughout this study.

The slope of the $S_L = S_L(t)$ curve, as well as S_L^{max} , provide a global yet rough description of the flow. The characterisation can be carried further by giving a more localised definition. Let us consider a section A of surface $|A|$ whose normal vector is along the imposed flow-rate (Fig.4). At a given time t , this section contains a liquid surface $|A_L|$. This allows to define a local saturation $s_L(A)$ associated with section A as:

$$s_L(A) = \frac{|A_L|}{|A|} \quad (13)$$

This provides a time characterisation of the flow that also depends on the position. The $s_L(A)$ values are expected to be zero as long as the flow does not reach the section under consideration. Then a transition until a maximum value $s_L^{max}(A)$ should occur [18]. This value allows to characterise the steady flow that sets in section A . The transition time between the transient and steady states thus give an information about the local dynamics of the flow. However, it is more suitable to deal with a space variable as retrieving a physical time from numerical simulation of two-phase flow can be difficult [43, 54]. In the literature, local saturation is expressed as a function of the position considering that each section reaches full saturation. This assumption does not hold here as the void content at final state is not necessarily negligible. This leads to introduce the following quantity R :

$$R(t; A) = \frac{s_L(t; A)}{s_L^{max}(A)} \quad (14)$$

691 It describes, at time t and for a given section A , how reached the steady
 692 state is. As a consequence, $R = 0$ indicates that the fluid has not reached the
 693 section A yet. Inversely, the value $R = 1$ means that the flow is steady. For
 694 any value between 0 and 1, the flow is considered as transient. The value of
 695 R can be represented at a given time t as a function of the section position.
 696 Assuming an imbibition from the left side to the right one as depicted in
 700 Fig.4, $R(A; t)$ is expected to go from 1 to 0. The transition zone between
 701 those asymptotic values is associated to a *saturation length* ℓ_s corresponding
 702 to partially saturated zone. As the poral structure is isotropic, we expect this
 703 saturation length to stabilise towards a constant value. Even if the volume
 704 does not reach the rigorous RVE size, ℓ_s should be compared to the domain
 705 characteristic length so as to give first conclusions about the separation of
 706 scales.

713 **2.2.2 Resulting capillary pressure**

714 The resulting capillary pressure is here computed at the interface level from
 715 Eqs. 7 and 8. The methods to evaluate these quantity in practice are now
 716 detailed. An expression for the macroscopic capillary pressure is first obtained
 717 from the average pressure jump at the interface (Eq.7). To do so, elements of
 718 the mesh that are cut by the interface (i.e. the zero iso-value of the ϕ field)
 719 are scanned. For each one, the difference of mean pressure on either side of
 720 the interface is computed. This gives a distribution of local capillary pressure
 721 from which the median value is taken. This quantity will be referred to as
 722 *pressure jump* capillary pressure and denoted as P_p^c .

723 A second possibility to compute the capillary pressure is to consider the
 724 average mean curvature (Eq.8). Such an approach is usually avoided as it
 725 requires a double derivative computation which is numerically sensitive. As the
 726

liquid-vapor interface is generally non-continuous and fragmented, one must first isolate each continuous piece of Γ_{LV} . Considering the linear approximation of the fields, every interface piece corresponds to a small set of continuous segments which have first to be smoothed so that the mean curvature can be computed.

As a method suitable for small dataset while providing a good smoothing of the curves, a Gaussian Process Regression (GPR) technique is here selected [46, 55, 56]. Here, each continuous piece of interface is seen as a parametric curve. For each one, a GPR is carried out with the arc length as input and each cartesian coordinates as outputs. Then the mean curvature can be easily computed for each continuous piece of the interface. This yields a distribution of mean curvature from which the median value is taken to retrieve a representative scalar quantity. This will be referred to as *mean curvature capillary pressure* and denoted as P_C^c . Despite the efficiency of the method, a considerable number of GPRs is required leading to significant computational costs.

Those methods for computing the interfacial capillary pressure are validated with the following test case: a 2D bubble with a unitary radius (i.e. a unitary curvature) is placed in a square domain (Fig.5). As a unitary surface tension coefficient is chosen, the capillary pressure is expected to be equal to one. In addition, a very low pressure drop is prescribed on the volume to make the bubble move slightly on the fixed mesh (Fig.5). As the pressure drop has a low intensity, no geometrical change of the bubble is observed and a simple translation occurs. This aims at assessing the robustness of the methods throughout the simulation.

The results of both methods are compared in Fig.6 for a given mesh. The relative error with respect to the expected unitary capillary pressure is plotted.

737
738
739
740
741
742
743
744
745
746
747
748
749
750
751
752
753
754
755
756
757
758
759
760
761
762
763
764
765
766
767
768
769
770
771
772
773
774
775
776
777
778
779
780
781
782

783 As for all the presented graphs, time t is normalised by the final time t_f . Even
 784 though both curves show a certain variability, it lies under 1% in absolute
 785 value. Furthermore, the median error for both capillary pressures gives very
 786 satisfactory results. The mesh convergence has also been studied as represented
 787 in Fig.7. As expected, the finer the mesh, the smaller the error. It should be
 788 remarked that mean curvature capillary pressure gives more precise results for
 789 a given mesh. The technique is especially very performing for coarse meshes.
 790 As regards the pressure jump capillary pressure, the precision of the method is
 791 enhanced by the enrichment of the elements cut by interface [43, 57]. Finally,
 792 both methods quickly converge towards the expected theoretical value. This
 793 gives us confidence in both of the proposed approaches.

801
802
803

804 **2.2.3 Statistical description of the flow front**

805

806 A new method to define the flow front position in the homogenised equivalent
 807 representation is now detailed. The main idea is to assume that the tran-
 808 sient behaviour is only localised in a band, the characteristic length of which
 809 corresponds to the flow front width, as depicted in Fig.8. Outside this area,
 810 the behaviour is assumed to be steady. Indeed, a static equilibrium between
 811 phases is supposed to be met upstream while the fluid have not reached the
 812 downstream area yet. Inside \mathcal{F} (Fig.8), the liquid-vapor interface is generally
 813 non-continuous. The presented approach considers the position of the inter-
 814 face within \mathcal{F} through a statistical description. Considering our numerical
 815 approach, the interface corresponds to a set of segments for which endpoints
 816 position are denoted as $\mathbf{x}_i^{\mathcal{F}} = (x_i^{\mathcal{F}}, y_i^{\mathcal{F}})$. The coordinate that follows the flow
 817 direction is considered as a realisation of a random variable. In the example
 818 described in Fig.8, this corresponds to the abscissa of the points that compose
 819 the interface and it is denoted as $I_{x^{\mathcal{F}}}$. This random variable is expected to

follow a Gaussian law, as the interface is mainly centred around a certain position and its density then decays symmetrically from it.

This method requires the identification of the flow front which can be difficult in practice. Here, the domain is divided into rectangles in the direction of flow (Fig.9). For each rectangle, the most downstream point of the interface is fetched (\mathbf{x}^* for the dark blue rectangle in Fig.9) and its associated piece of interface is retrieved (the green piece of interface in Fig.9). This method allows a good reconstruction of the interface even if some errors of attribution may occur (Fig.10).

3 Results

Results obtained through the methods detailed previously are now presented. Transient two-phase flow simulations have been carried out in a numerically generated fibrous microstructure with a fibre density V_f equal to 50% and a capillary number Ca equal to 10^{-3} . **This value is frequently chosen in the composite materials community as it has been shown to minimise the vapor content at final state, optimising therefore the impregnation quality [58, 59].**

3.1 Global and local saturations

The global saturation S_L is first considered. An example of temporal evolution for S_L has been represented in Fig.11. As noticed previously, such a curve shows two regimes: a linear transient phase and a subsequent convergence towards a two-phase equilibrium as the liquid has filled-in the volume. Despite the simplicity of this behaviour, several upscaling descriptors with physical meaning can be extracted. The slope of the first phase can be computed to characterise the global dynamics of the flow. Then, the time to reach stability may be compared between different microstructures with the same fibre

875 density and simulation parameters. At last, the asymptotic saturation value
 876 S_L^{max} corresponds to the residual proportion of vapor phase which is usually
 877 referred to as a void content in the composite materials community. Due to the
 878 flow incompressibility hypothesis, S_L^{max} may overestimate the experimentally
 879 observed values as density inside bubbles cannot change. These three descrip-
 880 tors (i.e. saturation curve slope, filling time and maximum saturation) will be
 881 studied more precisely through a statistical further study.

886 Saturation defined at section level is now under consideration. It can be first
 887 represented as a function of time for different sections of a same geometry. The
 888 observed behaviour follows the expected sigmoid as represented in Fig.12 for
 889 three given sections. As noticed previously, it is suitable to transpose the curve
 890 into the spatial domain to retrieve a saturation length. This has been achieved
 891 by considering the ratio R introduced in Section 2.2.1 as depicted in Fig.13 at
 892 three given times. From the transition width of these curves, saturation length
 893 ℓ_s can be derived at any given time. As a consequence, it can be considered as
 894 time-dependent as depicted in Fig.14. To recover a representative scalar quan-
 895 tity, saturation length is considered to be globally stable around a finite value
 896 ℓ_s^* , represented by a dashed line in Fig.14. In the case under consideration, this
 897 saturation length value is found to be around $7.6\bar{r}$. This means that the RVE
 898 size is sufficient here for the flow to settle in steady regime.

908
909
910

911 **3.2 Resulting capillary pressure**

912

913 The resulting capillary pressure is computed throughout the simulation dura-
 914 tion. Both methods that have been presented previously are considered. The
 915 temporal evolution of P_p^c and P_C^c is represented in Fig.15.

916

917 It can be observed that both behaviours are in very close agreement. The
 918 curves eventually converge towards very similar asymptotic values. These will
 919
920

be denoted by a star in exponent (i.e. P_p^{c*} and P_C^{c*}). We have here:

$$P_p^{c*} \approx P_C^{c*} = 12.7 \text{ kPa} \quad (15)$$

The time to reach stability can be interpreted as the time necessary to loose memory of the initialisation state. A certain amount of time is therefore required to reach a physically consistent state. This is the behaviour of a statistically isotropic porous medium [46], however stability might not be met for more complex poral structure materials [44]. Comparing Fig.11 and Fig.15, it must be noticed that the capillary pressures P_p^c and P_C^c converge while the global saturation is not stable yet. This shows that interface-defined capillary pressure becomes here independent of both time and saturation.

The results are in agreement with other recent works in which capillary pressure defined at the interface level tends to converge after a certain time. This reinforces the idea that capillary pressure, as defined here, can be considered as a function of the geometry and the interface properties only. Based on such a definition, it can be regarded as independent on the saturation. Consequently, considering an interfacial capillary pressure avoids the use of saturation-capillary pressure relationship which limits have been highlighted previously.

3.3 Statistical description of the flow front

A methodology to describe the flow front in terms of probability of presence has been described in Section 2.2.3. An example of distribution of flow front at a given time t is represented in Fig.16. The distribution can be modeled by a Gaussian law $\mathcal{N}(\mu, \sigma; t)$ as justified in Section 2.2.3. However, this trend

967 is not necessarily clear in practice. Indeed, identifying precisely the flow front
968 can be difficult [60, 61]. Attribution errors such as depicted in Fig.10 may lead
969 to alter the observed distribution. Yet, such a modeling will be kept as a first
970 approach.
971

972
973 The temporal evolution of the flow front distribution is represented in Fig.17.
974 The mean value $\mu(t)$ shows a linear trend over time. The standard deviation
975 $\sigma(t)$ starts to increase before being roughly stable around a value σ^* . From
976 Fig.17, this asymptotic value is estimated at $\sigma^* = 5.6\bar{r}$.
977
978
979

980

981

982 4 Discussion

983

984

985 Results from the proposed upscaling procedure have been presented in the
986 previous section. These have now to be compared to experimental observations
987 or to other numerical studies.
988

989

990

991 4.1 Saturation

992

993

994 Analogous curves to those represented in Fig.11 can be found in the litera-
995 ture for similar boundary conditions [17, 18]. Even for different geometries
996 and scales, as long as a flow rate is prescribed, the saturation increases lin-
997 early until reaching a plateau. Asymptotic saturation value S_L^{max} should also
998

999
1000 be compared to void content obtained in other study for similar Ca . However,
1001

1002 most of the contributions on fibrous media set at an intermediate mesoscopic
1003 scale: a dual-scale medium is thus considered as the liquid phase flows within
1004 and around yarns (i.e. bundle of fibres) [16, 17, 58, 62, 63]. This work focuses
1005 more specifically on the fibre scale: only microvoids are studied here.
1006

1007
1008 The fraction of residual vapor phase retrieved here is significantly higher than
1009 values commonly found in the literature. These generally lie between 1% and
1010 10% for similar capillary numbers. It should be noticed that fibre fraction
1011
1012

within yarns can reach really high values, around 75% [44]. For such a compact- 1013
 ity, the fibrous arrangement tends towards a regular hexagonal packing. This 1014
 entails an overall regular advancement of the flow front and thus a lower final 1015
 void content. Moreover, further mechanisms such as air compressibility and 1016
 dissolution [60] tend also to diminish the residual proportion of vapor phase. 1017
 As regards local saturation, making a comparison with other studies can be 1018
 complex. Indeed, most of them are located at a mesoscale involving a much 1019
 larger saturation length. Here, the computed saturation length is around 25 1020
 μm for a mean fibre radius of 3.5 μm . Considering the directly upper scale 1021
 on the order few millimeters [44], the scales seem to be well separated. This 1022
 means that at upper scales, the width of the unsaturated zone present at fi- 1023
 bre scale can be neglected. In other terms, in 2D, the moving interface within 1024
 the yarns can be wisely modeled by a 1D front in the equivalent homogeneous 1025
 medium as it can be done with a level-set method. 1026
 1027
 1028
 1029
 1030
 1031
 1032
 1033
 1034
 1035
 1036
 1037
 1038

4.2 Capillary pressure

A consistency between both methods to assess a resulting capillary pressure has 1039
 been shown previously. Close asymptotic values are thus obtained and should 1040
 be now compared to experimental results. Capillary pressure assessment in fi- 1041
 brous media has been a concern of the composite materials community over 1042
 the past twenty years [7, 36, 63–65]. However, a huge dispersion of the results 1043
 can be observed in practice as depicted in Fig.15. Therefore, the comparison 1044
 of our results with those found in the literature can be a difficult task, espe- 1045
 cially because fibre volume ratio or the geometries can be different. However, 1046
 the orders of magnitude remain consistent. Moreover, the mean value of the 1047
 capillary pressure results found in the literature is 12.2 kPa. This value is very 1048
 close to the asymptotic capillary pressure retrieved in this study (Eq.15). In 1049
 1050
 1051
 1052
 1053
 1054
 1055
 1056
 1057
 1058

1059 addition, it seems appropriate to consider some of the presented experimental
 1060 results as relevant bounds for capillary pressure. Considering Fig.15, results
 1061 from [64] represents a relevant lower bound while Pucci *et al.* measurements
 1062 from [64] represents a relevant lower bound while Pucci *et al.* measurements
 1063 [7] give a satisfactory upper bound.

1065 Analytical models have been also established to assess capillary pressure within
 1066 fibrous media [66–71]. The macroscopic contribution of capillary pressure is
 1067 then expressed as:

$$1070 \quad P_c = \frac{\gamma_{SV} - \gamma_{SL}}{r} \frac{V_f}{1 - V_f} \quad (16)$$

1071 where r is the fibre radius. For our material data and replacing r by the
 1072 mean fibre radius \bar{r} , this equation (Eq.16) estimates the resulting capillary
 1073 pressure at 8.2 kPa as represented in Fig.15. Even if this value is lower than
 1074 ours, it provides a satisfactory estimation. Indeed, we are considering here a
 1075 single random microstructure: a further statistical assessment of the capillary
 1076 pressure should be performed. In addition, the stochasticity of the geometry
 1077 under consideration (i.e. radius randomness, fibre position randomness,...) may
 1078 alter the expression of Eq.16.

1086
 1087

1088 **4.3 Statistical description of the flow front**

1089
 1090

1091 In Section 3.3, the flow front distribution has been characterised by a Gaussian
 1092 law. The advancement of distribution mean value has been shown to be linear
 1093 over time for flow rate inlet control conditions. This is consistent with the
 1094 saturation curve represented in Fig.11. We can thus write:

1095
 1096

$$1097 \quad \mu(t) \propto S_L(t) \quad (17)$$

1098
 1099

1100 The standard deviation $\sigma(t)$ of the flow front distribution can be physically
 1101 interpreted as a bandwidth within which the transient behaviour is contained.

This is very close to the concept of saturation length that has been introduced previously. It should be remarked that both ℓ_s and σ^* have comparable values. Seeing these quantities as characteristic length for the transient behaviour, both approaches appear to be consistent. Once again, it can be concluded that the spread of the flow front can be neglected at upper scales. This may justify the use of deterministic approach at both mesoscale and macroscale. Moreover, this reaffirms the relevance of considering a sharp interface at upper scales. This conclusion directly depends on the kind of porous medium under consideration as well as the flow parameters such as the capillary number [25]. In a more general case, the tools presented here provide a detailed description of the flow and give a thorough upscaling procedure.

Finally, in the context of this work, results arising from saturation (Section 3.1) and from the consideration of a flow front distribution (Section 3.3) are in close agreement. As noticed previously, this latter technique requires the identification of the flow front which can be challenging in practice. As a result, it seems preferable to use saturation-based methods for similar porous media and flow settings.

4.4 SRVEs and statistical mechanical response

In Section 2.1.3, the microstructures under consideration have been qualified as Statistical Representative Volume Elements, following the results from a previous study [46] and the definition from [52]. Indeed, our geometries are randomly generated and have been found to provide both a mechanical and geometrical representativity. In other words, given the SRVE nature of the generated geometries, the mechanical response of a single microstructure will be representative of a whole family of other geometries generated with similar

1151 fibre ratio volume and with analogous flow conditions.

1152 To illustrate it, the response of six randomly generated volumes with V_f equal
1153 to 50% are presented in Fig.18 and Fig.19, for $Ca = 10^{-3}$. It can be seen that
1154 the responses are indeed very close, both in terms of saturation or capillary
1155 pressure, even if an intrinsic dispersion is naturally observed. Since the present
1156 work aims at demonstrating the basics of the stochastic upscaling methodol-
1157 ogy dedicated to transient flows in composites manufacturing, a single SRVE
1158 has been considered. Obviously, a more exhaustive study is requested to fur-
1159 ther investigate the statistical upscaled flows in the space of the physical and
1160 geometrical descriptors.
1161
1162
1163
1164
1165
1166

1170 5 Conclusion

1171
1172 This work contributes to bridge the approaches developed by hydrogeology and
1173 composite materials communities in order to reach an upscaling method that
1174 is adapted to the impregnation of fibrous materials. From an in-depth anal-
1175 ysis of the methods encountered in literature, a re-examination of the usual
1176 upscaling descriptors has been performed, so that they can relevantly charac-
1177 terise the imbibition of fibrous materials.
1178
1179
1180

1181 From 2D SRVEs, flow simulations have been performed through a stabilised
1182 finite element method. Upscaling methods have been then identified from the
1183 developments of various scientific communities. Those have been adapted to
1184 the context of random fibrous media at microscale and further strategies have
1185 been proposed.
1186
1187
1188

1189 First, the notion of saturation, that usually describes the proportion of liquid
1190 within the poral space, has been considered both at volume and section scales.
1191 Their temporal and/or spatial evolution naturally leads to upscaling descrip-
1192 tors related to saturation dynamics or void content. Results are consistent and
1193
1194
1195
1196

the some identified discrepancies with the literature has been justified. Local 1197
saturation allows to determine a saturation length within which the transient 1198
behaviour is supposed to be contained. This length represents around 15% of 1199
the domain size. This allows us to conclude that the scales are well separated 1200
as the domain encompasses the entire transient behaviour. At upper scales, 1201
the width of the unsaturated zone may be neglected for the standard compos- 1202
ite materials under consideration. 1203
Then two methods have been proposed to assess a resulting capillary pressure 1204
from the interface behaviour. Both approaches have been validated on a test 1205
case and show an excellent agreement. A convergence of the capillary pressure 1206
is observed over time. It is thus independent of the saturation and only de- 1207
pends on the interface properties and inlet flow control. This may avoid the 1208
use of cumbersome relationship between saturation and capillary pressure. Our 1209
values of capillary pressure have been then shown to be in accordance with 1210
other analytical and experimental results. 1211
A novelty of this approach is to describe the flow front through a statistical 1212
modelling. After identifying the position of the flow front, a presence distribu- 1213
tion of the flow front is retrieved. In a first approach, this can be considered 1214
as a Gaussian law whose parameters behaviour are consistent with our pro- 1215
posed approach. In the situation under consideration, the spread parameter 1216
of the distribution is significantly lower than the characteristic length of the 1217
upper scale. This again justifies deterministic modeling of the flow front at up- 1218
per scales, for fibrous materials in the context of direct manufacturing processes. 1219
However, in the case of larger anisotropic porous media, the distribution spread 1220
may not be negligible anymore and the proposed statistical characterisation 1221
may be particularly relevant. 1222
Finally, the proposed strategy allows a thorough upscaling of the microscopic 1223
1224
1225
1226
1227
1228
1229
1230
1231
1232
1233
1234
1235
1236
1237
1238
1239
1240
1241
1242

1243 behaviour while justifying or reappraising some of the usual methods found
1244 in the literature. Both capillary number and fibre volume ratio has been kept
1245 constant here. Further studies should consider them as input variables of a
1246 more comprehensive model in which the presented upscaling descriptors are
1247 the output. This will allow to build a dataset so as to perform a more com-
1248 plete statistical characterisation of the upscaling.

1253 This contribution focuses on the upscaling methods so as to retrieve a novel
1254 procedure that is suited for the impregnation of fibrous materials. The up-
1255 scaling descriptors that have been highlighted are mostly scalar quantities
1256 and provide a thorough macroscopic characterisation of the flow under con-
1257 sideration. In future contributions, the influence of the flow settings and pore
1258 structure (*i.e.* Ca and V_f) on those descriptors will be investigated in order to
1259 extract constitutive laws ruling the imbibition of fibrous structures.

1264
1265
1266
1267

1268 References

1269
1270
1271
1272
1273
1274
1275
1276
1277
1278
1279
1280
1281
1282
1283
1284
1285
1286
1287
1288

- [1] Yan, G., Li, Z., Galindo Torres, S., Scheuermann, A., Li, L.: Transient Two-Phase Flow in Porous Media: A Literature Review and Engineering Application in Geotechnics. *Geotechnics* 2022, 2, 32–91 (2022)
- [2] Whitaker, S.: Flow in porous media i: A theoretical derivation of darcy’s law. *Transport in porous media* **1**(1), 3–25 (1986)
- [3] Hassanizadeh, S.M., Gray, W.G.: Toward an improved description of the physics of two-phase flow. *Advances in Water Resources* **16**(1), 53–67 (1993)
- [4] Michaud, V.: A review of non-saturated resin flow in liquid composite moulding processes. *Transport in porous media* **115**(3), 581–601 (2016)

- [5] Bodaghi, M., Lomov, S., Simacek, P., Correia, N., Advani, S.: On the variability of permeability induced by reinforcement distortions and dual scale flow in liquid composite moulding: A review. *Composites Part A: Applied Science and Manufacturing* **120**, 188–210 (2019)
- [6] Darcy, H.: *Les fontaines publiques de la ville de dijon: exposition et application...* (1856)
- [7] Pucci, M.F., Liotier, P.-J., Drapier, S.: Capillary wicking in a fibrous reinforcement–orthotropic issues to determine the capillary pressure components. *Composites Part A: Applied Science and Manufacturing* **77**, 133–141 (2015)
- [8] Teixidó, H., Staal, J., Caglar, B., Michaud, V.: Capillary effects in fiber reinforced polymer composite processing: A review. *Front. Mater.* **9**: 809226. doi: 10.3389/fmats (2022)
- [9] Kalaydjian, F.: A macroscopic description of multiphase flow in porous media involving spacetime evolution of fluid/fluid interface. *Transport in Porous Media* **2**(6), 537–552 (1987)
- [10] Hassanizadeh, S.M., Gray, W.G.: Mechanics and thermodynamics of multiphase flow in porous media including interphase boundaries. *Advances in water resources* **13**(4), 169–186 (1990)
- [11] Whitaker, S.: Flow in porous media ii: The governing equations for immiscible, two-phase flow. *Transport in porous media* **1**(2), 105–125 (1986)
- [12] Ambekar, A.S., Matthey, P., Buwa, V.V.: Pore-resolved two-phase flow in

- 1335 a pseudo-3d porous medium: Measurements and volume-of-fluid simula-
1336 tions. *Chemical Engineering Science* **230**, 116128 (2021)
1337
1338
- 1339 [13] Kuentzer, N., Simacek, P., Advani, S.G., Walsh, S.: Correlation of void dis-
1340 tribution to vartm manufacturing techniques. *Composites Part A: applied*
1341 *science and manufacturing* **38**(3), 802–813 (2007)
1342
1343
- 1344 [14] Gopala, V.R., van Wachem, B.G.: Volume of fluid methods for immiscible-
1345 fluid and free-surface flows. *Chemical Engineering Journal* **141**(1-3), 204–
1346 221 (2008)
1347
1348
- 1349 [15] Labat, L., Grisel, M., Breard, J., Bouquet, G.: Original use of elec-
1350 trical conductivity for void detection due to injection conditions of
1351 composite materials. *Comptes Rendus de l'Académie des Sciences-Series*
1352 *IIB-Mechanics* **329**(7), 529–534 (2001)
1353
1354
- 1355 [16] Park, C.H., Lebel, A., Saouab, A., Bréard, J., Lee, W.I.: Modeling and
1356 simulation of voids and saturation in liquid composite molding processes.
1357 *Composites Part A: Applied science and manufacturing* **42**(6), 658–668
1358 (2011)
1359
1360
- 1361 [17] Villière, M., Guérault, S., Sobotka, V., Boyard, N., Bréard, J., Delaunay,
1362 D.: Dynamic saturation curve measurement in liquid composite mold-
1363 ing by heat transfer analysis. *Composites Part A: Applied Science and*
1364 *Manufacturing* **69**, 255–265 (2015)
1365
1366
- 1367 [18] Gascón, L., García, J., LeBel, F., Ruiz, E., Trochu, F.: Numerical predic-
1368 tion of saturation in dual scale fibrous reinforcements during liquid com-
1369 posite molding. *Composites Part A: Applied Science and Manufacturing*
1370 **77**, 275–284 (2015)
1371
1372
- 1373
1374
1375
1376
1377
1378
1379
1380

- [19] Nordlund, M., Michaud, V.: Dynamic saturation curve measurement for resin flow in glass fibre reinforcement. *Composites Part A: Applied Science and Manufacturing* **43**(3), 333–343 (2012)
- [20] Fischer, R., Schlepütz, C.M., Hegemann, D., Rossi, R.M., Derome, D., Carmeliet, J.: Four-dimensional imaging and free-energy analysis of sudden pore-filling events in wicking of yarns. *Physical Review E* **103**(5), 053101 (2021)
- [21] Hassanizadeh, S.M., Gray, W.G.: Thermodynamic basis of capillary pressure in porous media. *Water resources research* **29**(10), 3389–3405 (1993)
- [22] Van Genuchten, M.T.: A closed-form equation for predicting the hydraulic conductivity of unsaturated soils. *Soil science society of America journal* **44**(5), 892–898 (1980)
- [23] Hassanizadeh, S.M., Celia, M.A., Dahle, H.K.: Dynamic effect in the capillary pressure–saturation relationship and its impacts on unsaturated flow. *Vadose Zone Journal* **1**(1), 38–57 (2002)
- [24] Armstrong, R.T., Porter, M.L., Wildenschild, D.: Linking pore-scale interfacial curvature to column-scale capillary pressure. *Advances in Water resources* **46**, 55–62 (2012)
- [25] Ferrari, A., Lunati, I.: Direct numerical simulations of interface dynamics to link capillary pressure and total surface energy. *Advances in water resources* **57**, 19–31 (2013)
- [26] Schlüter, S., Berg, S., Li, T., Vogel, H.-J., Wildenschild, D.: Time scales of relaxation dynamics during transient conditions in two-phase flow. *Water*

- 1427 Resources Research **53**(6), 4709–4724 (2017)
1428
- 1429 [27] Camps-Roach, G., O’Carroll, D.M., Newson, T.A., Sakaki, T., Illan-
1430 gasekare, T.H.: Experimental investigation of dynamic effects in capillary
1431 pressure: Grain size dependency and upscaling. *Water Resources Research*
1432 **46**(8) (2010)
1433
1434
1435
1436
- 1437 [28] Joekar-Niasar, V., Hassanizadeh, S.M.: Effect of fluids properties on
1438 non-equilibrium capillarity effects: Dynamic pore-network modeling. *Inter-
1439 national Journal of Multiphase Flow* **37**(2)
1440
1441
1442
- 1443 [29] Dahle, H.K., Celia, M.A., Majid Hassanizadeh, S.: Bundle-of-tubes model
1444 for calculating dynamic effects in the capillary-pressure-saturation rela-
1445 tionship. *Transport in Porous media* **58**(1), 5–22 (2005)
1446
1447
1448
- 1449 [30] Cai, J.-C., Chen, Y., Qiao, J.-C., Yang, L., Zeng, J.-H., Sun, C.-H.: Deter-
1450 mination of dynamic capillary effect on two-phase flow in porous media:
1451 A perspective from various methods. *Petroleum Science* (2022)
1452
1453
- 1454 [31] Bottero, S., Hassanizadeh, S.M., Kleingeld, P.: From local measurements
1455 to an upscaled capillary pressure–saturation curve. *Transport in Porous
1456 Media* **88**(2), 271–291 (2011)
1457
1458
1459
- 1460 [32] Joekar-Niasar, V., Hassanizadeh, S.M., Dahle, H.: Non-equilibrium effects
1461 in capillarity and interfacial area in two-phase flow: dynamic pore-network
1462 modelling. *Journal of Fluid Mechanics* **655**, 38–71 (2010)
1463
1464
1465
- 1466 [33] Konangi, S., Palakurthi, N.K., Karadimitriou, N.K., Comer, K., Ghia,
1467 U.: Comparison of pore-scale capillary pressure to macroscale capillary
1468 pressure using direct numerical simulations of drainage under dynamic
1469 and quasi-static conditions. *Advances in Water Resources* **147**, 103792
1470
1471
1472

- (2021) 1473
1474
- [34] Starnoni, M., Pokrajac, D.: On the concept of macroscopic capillary pressure in two-phase porous media flow. *Advances in Water Resources* **135**, 103487 (2020) 1475
1476
1477
1478
1479
1480
- [35] Shokri, J., Godinez-Brizuela, O.E., Erfani, H., Chen, Y., Babaei, M., Berkowitz, B., Niasar, V.: Impact of displacement direction relative to heterogeneity on averaged capillary pressure-saturation curves. *Water Resources Research* **58**(2), 2021–030748 (2022) 1481
1482
1483
1484
1485
1486
1487
1488
- [36] Willenbacher, B., May, D., Mitschang, P.: Out-of-plane capillary pressure of technical textiles. *Composites Part A: Applied Science and Manufacturing* **124**, 105495 (2019) 1489
1490
1491
1492
1493
1494
- [37] Chevalier, L., Bruchon, J., Moulin, N., Liotier, P.-J., Drapier, S.: Accounting for local capillary effects in two-phase flows with relaxed surface tension formulation in enriched finite elements. *Comptes Rendus Mécanique* **346**(8), 617–633 (2018) 1495
1496
1497
1498
1499
1500
1501
- [38] Pucci, M.F., Liotier, P.-J., Drapier, S.: Tensiometric method to reliably assess wetting properties of single fibers with resins: Validation on cellulosic reinforcements for composites. *Colloids and Surfaces A: Physicochemical and Engineering Aspects* **512**, 26–33 (2017) 1502
1503
1504
1505
1506
1507
1508
- [39] Osher, S., Fedkiw, R.P.: Level set methods: an overview and some recent results. *Journal of Computational physics* **169**(2), 463–502 (2001) 1509
1510
1511
1512
1513
- [40] Shakoor, M., Scholtes, B., Bouchard, P.-O., Bernacki, M.: An efficient and parallel level set reinitialization method—application to micromechanics 1514
1515
1516
1517
1518

- 1519 and microstructural evolutions. *Applied Mathematical Modelling* **39**(23-
1520 24), 7291–7302 (2015)
1521
1522
- 1523 [41] Min, C.: On reinitializing level set functions. *Journal of computational*
1524 *physics* **229**(8), 2764–2772 (2010)
1525
1526
- 1527 [42] Blais, M., Moulin, N., Liotier, P.-J., Drapier, S.: Resin infusion-based
1528 processes simulation: coupled stokes-darcy flows in orthotropic preforms
1529 undergoing finite strain. *International Journal of Material Forming* **10**(1),
1530 43–54 (2017)
1531
1532
1533
- 1534 [43] Chevalier, L.: Accounting for capillary effects in level-set based finite ele-
1535 ments modelling of impregnation in fibrous media. PhD thesis, Université
1536 de Lyon (2019)
1537
1538
1539
- 1540 [44] Geoffre, A., Wielhorski, Y., Moulin, N., Bruchon, J., Drapier, S., Liotier,
1541 P.-J.: Influence of intra-yarn flows on whole 3d woven fabric numerical per-
1542 meability: from stokes to stokes-darcy simulations. *International Journal*
1543 *of Multiphase Flow* **129**, 103349 (2020)
1544
1545
1546
1547
- 1548 [45] Liu, Y., Moulin, N., Bruchon, J., Liotier, P.-J., Drapier, S.: Towards void
1549 formation and permeability predictions in lcm processes: a computational
1550 bifluid–solid mechanics framework dealing with capillarity and wetting
1551 issues. *Comptes Rendus Mécanique* **344**(4-5), 236–250 (2016)
1552
1553
1554
- 1555 [46] Geoffre, A., Ghestin, M., Moulin, N., Bruchon, J., Drapier, S.: Bound-
1556 ing transverse permeability of fibrous media: a statistical study from
1557 random representative volume elements with consideration of fluid slip.
1558 *International Journal of Multiphase Flow* **143**, 103751 (2021)
1559
1560
1561
1562
1563
1564

- [47] Abouorm, L., Troian, R., Drapier, S., Bruchon, J., Moulin, N.: Stokes–darcy coupling in severe regimes using multiscale stabilisation for mixed finite elements: monolithic approach versus decoupled approach. *European Journal of Computational Mechanics* **23**(3-4), 113–137 (2014)
- [48] Pacquaut, G., Bruchon, J., Moulin, N., Drapier, S.: Combining a level-set method and a mixed stabilized p1/p1 formulation for coupling stokes–darcy flows. *International Journal for Numerical Methods in Fluids* **69**(2), 459–480 (2012)
- [49] Codina, R.: A stabilized finite element method for generalized stationary incompressible flows. *Computer methods in applied mechanics and engineering* **190**(20-21), 2681–2706 (2001)
- [50] Hughes, T.J.: Multiscale phenomena: Green’s functions, the dirichlet-to-neumann formulation, subgrid scale models, bubbles and the origins of stabilized methods. *Computer methods in applied mechanics and engineering* **127**(1-4), 387–401 (1995)
- [51] Brooks, A.N., Hughes, T.J.: Streamline upwind/ Petrov-galerkin formulations for convection dominated flows with particular emphasis on the incompressible navier-stokes equations. *Computer methods in applied mechanics and engineering* **32**(1-3), 199–259 (1982)
- [52] Trias, D., Costa, J., Turon, A., Hurtado, J.: Determination of the critical size of a statistical representative volume element (srve) for carbon reinforced polymers. *Acta materialia* **54**(13), 3471–3484 (2006)
- [53] Kang, M.K., Lee, W.I., Hahn, H.T.: Formation of microvoids during resin-transfer molding process. *Composites Science and Technology* **60**(12-13),

1611 2427–2434 (2000)

1612

1613

1614

[54] Kunz, P., Zarikos, I., Karadimitriou, N., Huber, M., Nieken, U., Hasanizadeh, S.: Study of multi-phase flow in porous media: comparison of sph simulations with micro-model experiments. *Transport in Porous Media* **114**(2), 581–600 (2016)

1619

1620

1621

[55] Rasmussen, C.E.: Gaussian processes in machine learning. In: Summer School on Machine Learning, pp. 63–71 (2003). Springer

1622

1623

1624

1625

[56] Trochu, F.: A contouring program based on dual kriging interpolation.

1626

1627

Engineering with computers **9**(3), 160–177 (1993)

1628

1629

[57] Ausas, R.F., Buscaglia, G.C., Idelsohn, S.R.: A new enrichment space for the treatment of discontinuous pressures in multi-fluid flows. *International Journal for Numerical Methods in Fluids* **70**(7), 829–850 (2012)

1630

1631

1632

1633

1634

1635

[58] Leclerc, J.S., Ruiz, E.: Porosity reduction using optimized flow velocity in resin transfer molding. *Composites Part A: Applied Science and Manufacturing* **39**(12), 1859–1868 (2008)

1636

1637

1638

1639

1640

[59] Ruiz, E., Achim, V., Soukane, S., Trochu, F., Bréard, J.: Optimization of injection flow rate to minimize micro/macro-voids formation in resin transfer molded composites. *Composites science and technology* **66**(3-4), 475–486 (2006)

1641

1642

1643

1644

1645

1646

1647

1648

[60] Park, C.H., Woo, L.: Modeling void formation and unsaturated flow

1649

1650

1651

1652

in liquid composite molding processes: a survey and review. *Journal of reinforced plastics and composites* **30**(11), 957–977 (2011)

1653

1654

1655

[61] Causse, P., Ravey, C., Trochu, F.: Capillary characterization of fibrous

1656

- reinforcement and optimization of injection strategy in resin transfer molding. *Journal of Composites Science* **2**(2), 19 (2018) 1657
1658
1659
1660
- [62] DeValve, C., Pitchumani, R.: Simulation of void formation in liquid composite molding processes. *Composites Part A: Applied Science and Manufacturing* **51**, 22–32 (2013) 1661
1662
1663
1664
1665
1666
- [63] Schell, J., Deleglise, M., Binetruy, C., Krawczak, P., Ermanni, P.: Numerical prediction and experimental characterisation of meso-scale-voids in liquid composite moulding. *Composites Part A: applied science and manufacturing* **38**(12), 2460–2470 (2007) 1667
1668
1669
1670
1671
1672
1673
1674
- [64] Amico, S., Lekakou, C.: An experimental study of the permeability and capillary pressure in resin-transfer moulding. *Composites Science and Technology* **61**(13), 1945–1959 (2001) 1675
1676
1677
1678
1679
- [65] Koubaa, S., Burtin, C., Le Corre, S.: Investigation of capillary impregnation for permeability prediction of fibrous reinforcements. *Journal of Composite Materials* **50**(11), 1417–1429 (2016) 1680
1681
1682
1683
1684
1685
- [66] Vilà, J., Sket, F., Wilde, F., Requena, G., González, C., LLorca, J.: An in situ investigation of microscopic infusion and void transport during vacuum-assisted infiltration by means of x-ray computed tomography. *Composites science and technology* **119**, 12–19 (2015) 1686
1687
1688
1689
1690
1691
1692
1693
- [67] Pillai, K.M., Advani, S.G.: Wicking across a fiber-bank. *Journal of colloid and interface science* **183**(1), 100–110 (1996) 1694
1695
1696
1697
- [68] Bayramli, E., Powell, R.: The normal (transverse) impregnation of liquids into axially oriented fiber bundles. *Journal of colloid and interface science* **138**(2), 346–353 (1990) 1698
1699
1700
1701
1702

- 1703 [69] Neacsu, V., Obaid, A.A., Advani, S.: Spontaneous radial capillary impreg-
1704 nation across a bank of aligned micro-cylinders—part i: Theory and model
1705 development. *International journal of multiphase flow* **32**(6), 661–676
1706 (2006)
1707
1708
1709
1710 [70] Ahn, K., Seferis, J., Berg, J.: Simultaneous measurements of perme-
1711 ability and capillary pressure of thermosetting matrices in woven fabric
1712 reinforcements. *Polymer composites* **12**(3), 146–152 (1991)
1713
1714
1715
1716 [71] Yeager, M., Hwang, W.R., Advani, S.G.: Prediction of capillary pressure
1717 for resin flow between fibers. *Composites Science and Technology* **126**,
1718 130–138 (2016)
1719
1720
1721

1722 **Statements and Declarations**

1723 The authors declare that no funds, grants, or other support were received dur-
1724 ing the preparation of this manuscript. The authors have no relevant financial
1725 or non-financial interests to disclose.
1726
1727
1728
1729
1730
1731
1732
1733
1734
1735
1736
1737
1738
1739
1740
1741
1742
1743
1744
1745
1746
1747
1748

γ_{SV} (N/mm)	γ_{SL} (N/mm)	γ_{LV} (N/mm)	η_V (Pa.s)	η_L (Pa.s)
54.7×10^{-3}	25.9×10^{-3}	50.8×10^{-3}	1.71×10^{-5}	2.76×10^{-3}

Table 1: Fluid properties chosen for the numerical simulations.

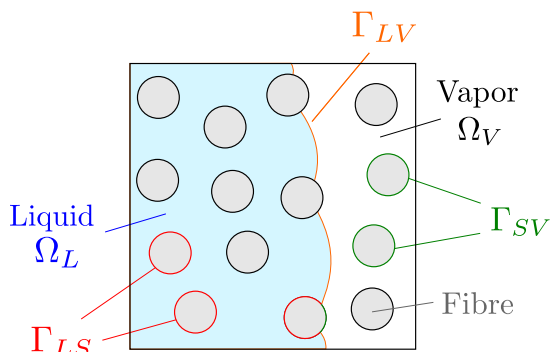


Figure 1: Imbibition in a fibrous medium: domains, boundaries and notations.

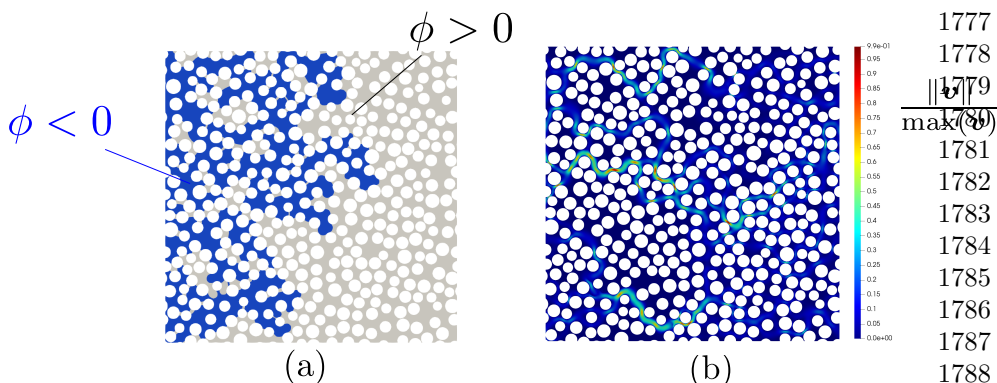
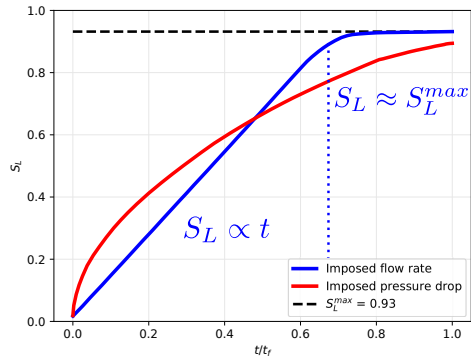


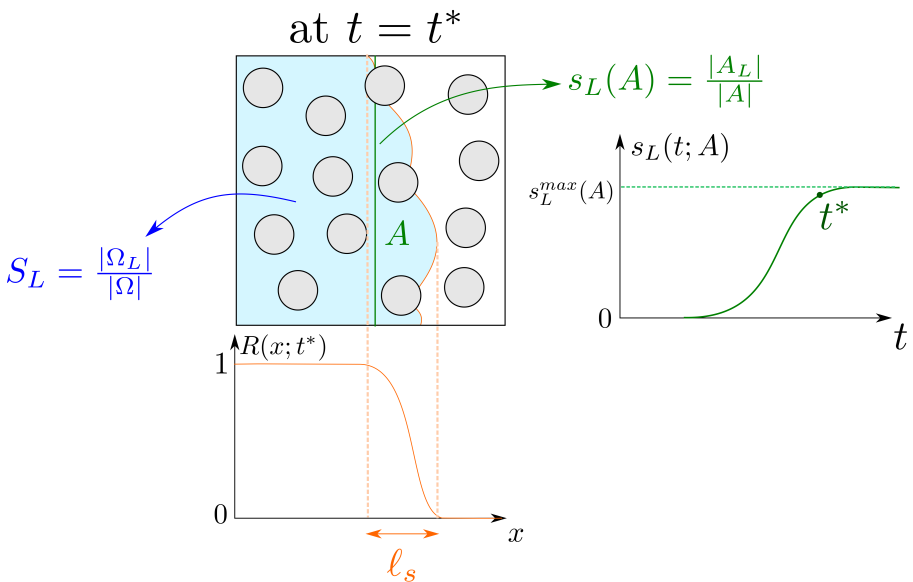
Figure 2: A simulation example of transient two-phase flow within a generated fibrous microstructure: (a) location of the phases (blue: liquid, grey: vapor), (b) normalised velocity magnitude.

1795
1796
1797
1798
1799
1800
1801
1802
1803
1804
1805
1806
1807
1808
1809



1810 **Figure 3:** Temporal evolution of global saturation S_L for different inlet
1811 boundary conditions.

1812
1813
1814
1815
1816
1817
1818
1819
1820
1821
1822
1823
1824
1825
1826
1827



1828
1829
1830
1831
1832
1833
1834
1835
1836
1837
1838
1839
1840

Figure 4: Notions of saturation and saturation length.

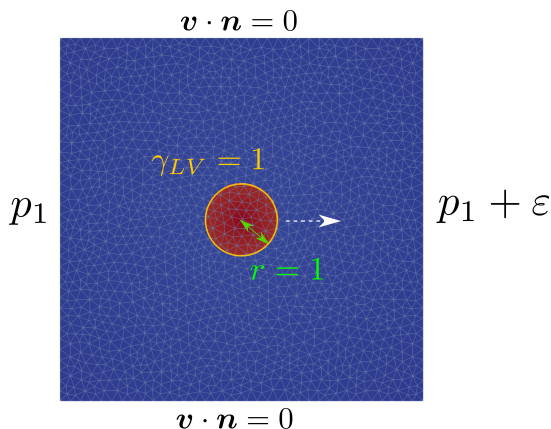


Figure 5: Test case for the validation of the resulting capillary pressure computation : parameters, boundary conditions and mesh (1655 nodes). A pressure of low intensity ϵ is prescribed.

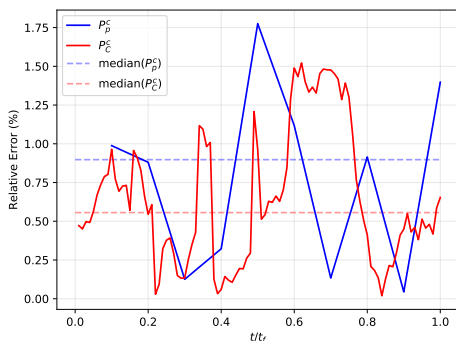


Figure 6: Relative error between reference value and the two methods to assess the resulting capillary pressure for a given mesh (1215 nodes).

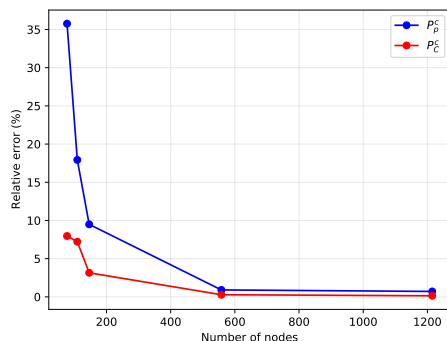


Figure 7: Mesh convergence for the two methods to assess the resulting capillary pressure.

1841
1842
1843
1844
1845
1846
1847
1848
1849
1850
1851
1852
1853
1854
1855
1856
1857
1858
1859
1860
1861
1862
1863
1864
1865
1866

1879
1880
1881
1882
1883
1884
1885
1886

1887

1888

1889

1890

1891

1892

1893

1894

1895

1896

1897

1898

1899

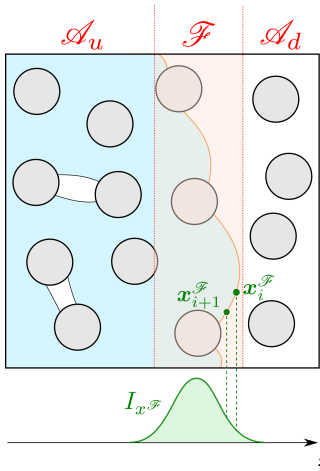
1900

1901

1902

1903

1904



1905 **Figure 8:** Statistical approach
1906 to describe the flow front.

1907

1908

1909

1910

1911

1912

1913

1914

1915

1916

1917

1918

1919

1920

1921

1922

1923

1924

1925

1926

1927

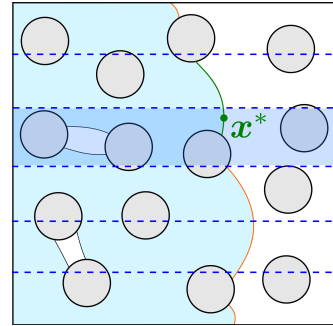
1928

1929

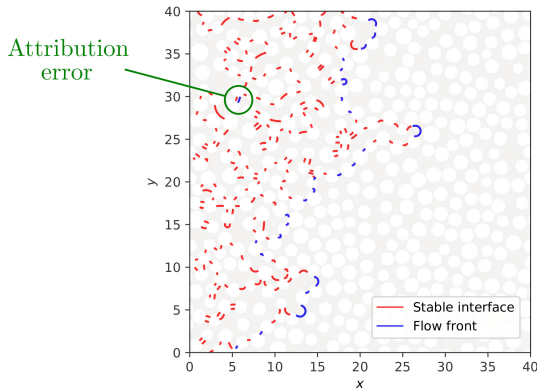
1930

1931

1932



1905 **Figure 9:** A method to identify
1906 the flow front.



1905 **Figure 10:** Example of flow front identification.

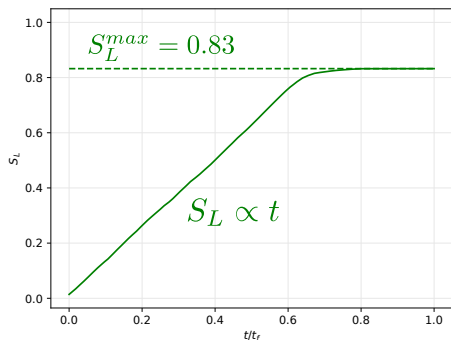


Figure 11: Temporal evolution of the global saturation.

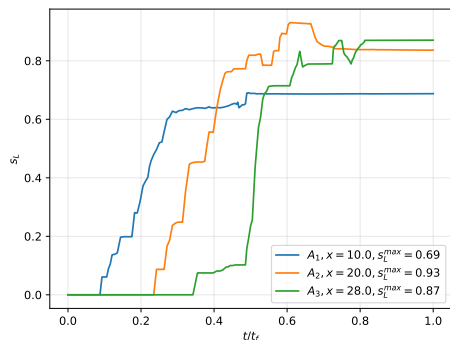


Figure 12: Temporal evolution of the saturation of three sections characterised by their abscissa x .

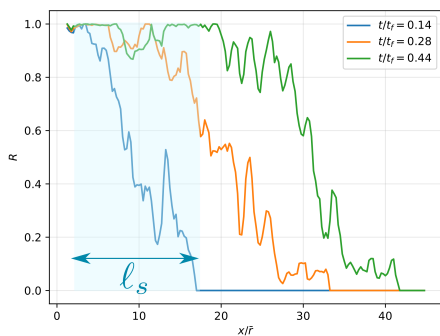


Figure 13: Spatial evolution of the ratio R for three given times.

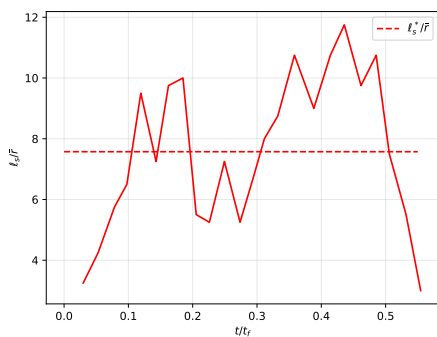


Figure 14: Temporal evolution of the saturation length normalised by the mean fibre radius.

1933
1934
1935
1936

1940
1949
1950
1951
1952
1953
1954
1955
1956
1957
1958
1959

1972
1973
1974
1975
1976
1977
1978

1979
 1980
 1981
 1982
 1983
 1984
 1985
 1986
 1987
 1988
 1989
 1990
 1991
 1992
 1993
 1994
 1995
 1996
 1997
 1998
 1999
 2000
 2001
 2002
 2003
 2004
 2005
 2006
 2007
 2008
 2009
 2010
 2011
 2012
 2013
 2014
 2015
 2016
 2017
 2018
 2019
 2020
 2021
 2022
 2023
 2024

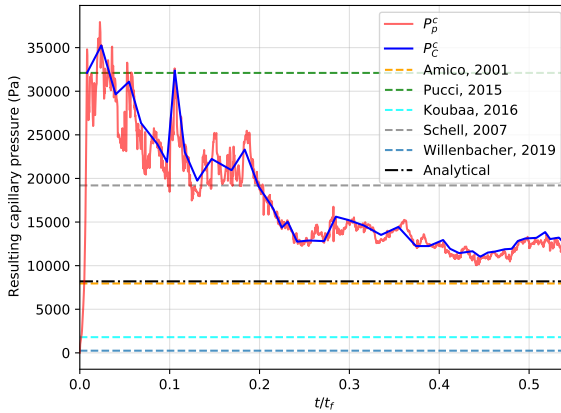


Figure 15: Temporal evolution of the resulting capillary pressure defined at the interface level: proposed methods and literature.

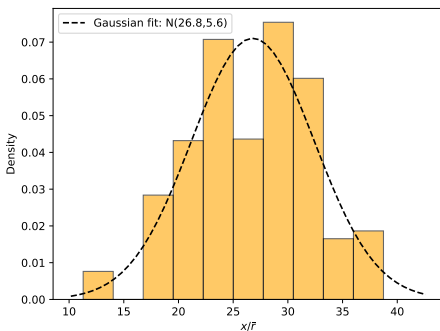


Figure 16: Distribution of flow front at $t/t_f = 0.73$.

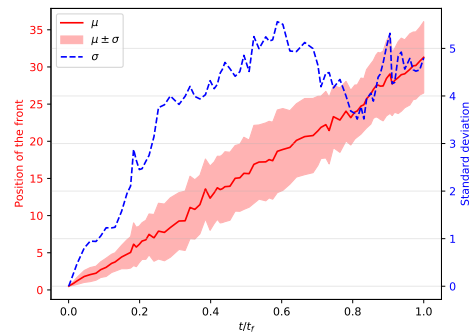


Figure 17: Distribution of flow front over time: mean value, dispersion and standard deviation.

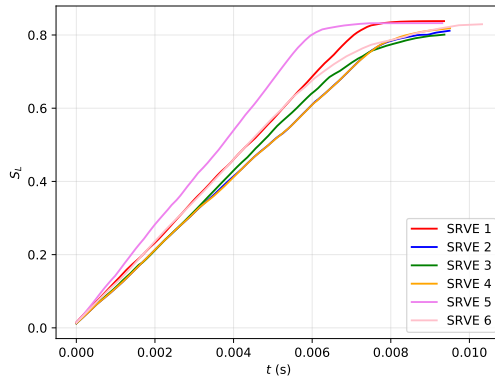


Figure 18: Time evolution of the global saturation for six randomly generated microstructures ($V_f = 50\%$, $Ca = 10^{-3}$).

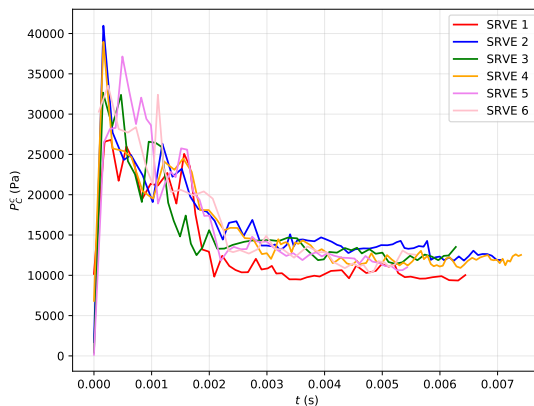


Figure 19: Time evolution of the resulting capillary pressure for six randomly generated microstructures ($V_f = 50\%$, $Ca = 10^{-3}$).

2025
2026
2027
2028
2029
2030
2031
2032
2033
2034
2035
2036
2037
2038
2039
2040
2041
2042
2043
2044
2045
2046
2047
2048
2049
2050
2051
2052
2053
2054
2055
2056
2057
2058
2059
2060
2061
2062
2063
2064
2065
2066
2067
2068
2069
2070